ISSN 1573-160X, *PHYSICAL OCEANOGRAPHY*, Vol. 33, Iss. 1, pp. 156-184 (2026)

Original article

# A Discrete Transport Equation with Nonlinear Invariants: Application to the Black Sea Circulation Modelling

**S. G. Demyshev ✉, O. A. Dymova**

*Marine Hydrophysical Institute of RAS, Sevastopol, Russian Federation*
✉ *demyshev@gmail.com*

*Abstract*

*Purpose*. The purpose of this study is to investigate a new approximation scheme for nonlinear terms in the heat and salt transport equations. It ensures the conservation of temperature in the first and $K^{th}$ ($K > 2$) degree, salinity in the first and $L^{th}$ ($L > 2$) degree and density as a polynomial in temperature and salinity. To evaluate the efficacy of the new scheme for modelling sea circulation under realistic boundary conditions.

*Methods and Results*. The new approximation is tested on the reconstruction of the Black Sea circulation using the MHI-model and ERA5 atmospheric forcing for 2016. The results show that the Cold Intermediate Layer becomes sharper and its depth decreases; similarly, the depth of the upper boundary of the permanent halocline is reduced. The modelling results are compared with *in-situ* data and the hydrophysical fields obtained by using a traditional approximation scheme. Validation of the results shows that the modelling error of the salinity fields decreases in the upper 100-m layer when the new scheme is used.

*Conclusions*. An approximation scheme for the heat and salt advection equations that preserves nonlinear invariants was developed and generalized to the case of a functional depending on two or more functions. The decrease in modelling errors is related to the refinement of seawater density gradients, vertical mixing coefficients and upwelling/downwelling velocities. Spectral analysis of the current kinetic energy and the vertical velocity demonstrates a more accurate redistribution of energy along the motion spectrum compared to data from the earlier version of the MHI-model.

**Keywords**: finite-difference approximation, nonlinear invariants, conservation laws, Black Sea, numerical modelling, thermohaline circulation, energy spectrum

**Acknowledgments:** This work was supported by the state assignment of the FSBSI FRC MHI, project No. FNNN-2024-0001.

**For citation:** Demyshev, S.G. and Dymova, O.A., 2026. A Discrete Transport Equation with Nonlinear Invariants: Application to the Black Sea Circulation Modelling. *Physical Oceanography*, 33(1), pp. 156-184.



## Introduction

A system of differential equations containing advection–diffusion equations is required to solve problems of studying the continuum dynamics. Effective methods for numerical solution of the advection–diffusion equation were developed in the second half of the 20th century. As demonstrated [1, 2], the properties of the discrete solution of the advection–diffusion equation depend on the method of the advective terms approximation. The solution can be distorted due to the manifestation of computational dispersion and viscosity, so it is necessary

to improve the dispersion and dissipation properties of the solution by searching for new directions in constructing difference schemes. Another important aspect concerns the need for correct approximation of nonlinear terms. In general ocean models, transport equations are usually discretized using schemes that ensure conservation of the transferred quantity and the square of this quantity [3–5]. At the same time, the sea water density is a polynomial of temperature and salinity of varying degrees in the case of insignificant influence of pressure [6]. Therefore, the discrete advection equation must have the property of preserving temperature, salinity and their various degrees. In the case of a nonlinear state equation, the property of conservation of the total discrete energy (kinetic plus potential) requires that the buoyancy work be described in the difference equations for kinetic and potential energy in the same way. In turn, this property is satisfied if the discrete density advection equation in divergence form is obtained as a consequence of the finite–difference equations for temperature and salinity.

An original approach for approximation of the advection equation is proposed in [7, 8]. Here, a new difference scheme, called the CABARET scheme, is presented for a one-dimensional transport equation. In the class of linear schemes, it is exact for two different values of the Courant–Friedrichs–Lewy condition lying in its stability region, which means the scheme does not contain approximation variance. The CABARET scheme is divergence form and satisfies conservation laws. In [9], it is implemented in the multilayer hydrostatic model CABARET–MFSH to solve a hyperbolic equations system. The model describes the dynamics of a fluid with variable density and free surface, and is used to simulate the propagation of internal waves. The results of numerical experiments are in satisfactory agreement with the experimental data.

In [10], combination of two or more explicit numerical schemes approximating the same transport equation and satisfying some conservation laws is considered. Numerical tests confirmed that the mixed scheme gives quite accurate results when the governing macroscopic and microscopic schemes are Eulerian and Lagrangian respectively. In [11], a discrete one-dimensional advection–diffusion equation is analyzed. The Crank–Nicolson scheme is used for time stepping, and the central differencing scheme is used for spatial discretization. The error of the scheme is calculated, and numerical characteristics of the convergence rate are obtained to assess the quality of the numerical solution. A method based on equivariant moving frames for developing highly invariant compact finite–difference schemes which preserve symmetry groups (or invariants) is presented in [12]. Application of the method is demonstrated by constructing invariant compact difference schemes for some linear and nonlinear advection–diffusion equations. The obtained results show that the invariant compact finite–difference schemes not only possess the symmetry properties of the underlying partial differential equations, but are also comparatively more accurate than standard schemes.

One way of creating the discrete transport equation is based on constructing schemes that have nonlinear invariants. If pressure is not taken into account, the density is calculated from the state equation, which is a polynomial of temperature and salinity. Therefore, not only temperature and salinity, but also the degrees of these functions corresponding to the state equation must be preserved in the difference formulation. In [13, 14], an approximation scheme of the heat and

salt advection equation possessing nonlinear invariants (degrees higher than two) is proposed, and relations providing a divergence form of the density advection equation are obtained. In order for the law of total energy (kinetic plus potential) conservation to be satisfied in the numerical model, an identical description of the buoyancy work in both energy equations is required. Its form follows from the third equation of motion for the kinetic energy equation, and it is due to vertical density advection for the potential energy equation. Therefore, it is necessary to derive a difference density equation, which is an exact consequence of the discrete heat and salt advection equations. It should have a divergence form and lead to the same form of the buoyancy work in the discrete equations for kinetic and potential energy. Thus, the exact fulfilment of the law of total energy conservation is ensured in the numerical model.

Numerical analysis of the kinetic and potential energy budget equations makes it possible to estimate the contributions of physical processes such as atmospheric forcing, instability, friction, and diffusion to the mechanisms of circulation variability in the oceans and seas. Bryan [15] was among the first to apply this approach, which has since become widely used in modern studies [16–18]. For the Black Sea, numerical estimates of the circulation energy budget components are presented in [19–21]. A comprehensive analysis of the hydrophysical, energetic, and spectral properties of the modelling results in conjunction with direct observational data enables to identify the effectiveness and/or shortcomings of the models used.

This work is a generalization and development of the results obtained earlier on the construction of an eddy-resolving ocean model with schemes possessing discrete nonlinear invariants. The aim of the study is to investigate the impact of a new approximation scheme of the heat and salt transport equations on the structure and variability of the Black Sea hydrophysical fields based on comparing modelling results with observations and previously obtained data.

## Approximation of transport equation

### Differential problem

Let us consider the fluid motion in the area Ω in the Cartesian coordinate system ($x$, $y$, $z$). Let $q$ be an invariant, i.e.,

$$\frac{dq}{dt} = 0. \tag{1}$$

Suppose that $Q(q)$ is a functional differentiable with respect to $q$. Then it follows from Eq. (1) that

$$\frac{dQ}{dt} = Q_t + uQ_x + vQ_y + wQ_z = 0, \tag{2}$$

hence, $Q$ is also an invariant. We assume that the fluid is incompressible and the continuity condition is satisfied:

$$u_x + v_y + w_z = 0. \tag{3}$$

Then Eq. (2) is rewritten as:

$$Q_t + (uQ)_x + (vQ)_y + (wQ)_z = 0.$$

If we set the normal velocity equal to zero at the boundaries, we obtain

$$\frac{\partial}{\partial t}\int\limits_{\Omega} q\, d\Omega = 0, \quad \frac{\partial}{\partial t}\int\limits_{\Omega} Q\, d\Omega = 0. \tag{4}$$

It is easy to generalize Eq. (4) to a sequence of invariants $q^r$ ($r$ is an index that varies from 1 to $R$), where each $q^r$ satisfies

$$(q^r)_t + (uq^r)_x + (vq^r)_y + (wq^r)_z = 0.$$

Let $Q = Q(q^1, \ldots, q^R)$ be differentiable with respect to each $q^r$. Then it follows that

$$\frac{\partial}{\partial t}\int\limits_{\Omega} q^r\, d\Omega = 0, \qquad \frac{\partial}{\partial t}\int_{\Omega} Q(q^1, \ldots, q^R) d\Omega = 0. \tag{5}$$

**Discrete problem**

Let us divide a rectangular basin with an uneven bottom and steep walls into elementary cells with centers corresponding to integer values of indices $i$, $j$, $k$ ($i$ = 1, …, $I$; $j$ = 1, …, $J$; $k$ = 1, …, $K_{i,j}$) and edges corresponding to half values of indices $i$ + 1/2, $j$ + 1/2, $k$ +1/2. The horizontal cells sizes $(h_x, h_y)$ are constant, the vertical size is a non-uniform approximation ($h_z^k = z_{k+1/2} - z_{k-1/2}$, $h_z^{k+1/2} = z_{k+1} - z_k$). The upper border is a free surface, the upper cell has a fixed size. The distribution scheme of prognostic variables corresponds to the *C*-grid [22] and is presented in Fig. 1. We introduce $x$, $y$, $z$ axes pointing eastward, northward and vertically downward, respectively.

Let φ be the integrating function. Introduce finite-difference operators (the same way for $j$, $k$):

$$\overline{\varphi}^{x}_{i,j,k} = \frac{\varphi_{i+1/2,j,k} + \varphi_{i-1/2,j,k}}{2}, \qquad \delta_x \varphi_{i,j,k} = \frac{\varphi_{i+1/2,j,k} - \varphi_{i-1/2,j,k}}{h_x},$$

$$\nabla^2_{x,y}\varphi_{i,j,k} = \delta^2_x \varphi_{i,j,k} + \delta^2_y \varphi_{i,j,k},$$

$$\{\varphi\}^V = \frac{1}{V}\sum_{i,j}\sum_{k=1}^{K_{i,j}} \varphi_{i,j,k} h_z^k h_x h_y, \qquad V = \sum_{i,j}\sum_{k=1}^{K_{i,j}} h_z^k h_x h_y, \tag{6}$$

here $\Omega_k$ is the area at $z_k$ horizon (Fig. 1), $V$ is volume. The temperature, salinity and horizontal velocities are calculated at $z_k$ horizons, vertical velocity is calculated at $z_{k+1/2}$ horizons.

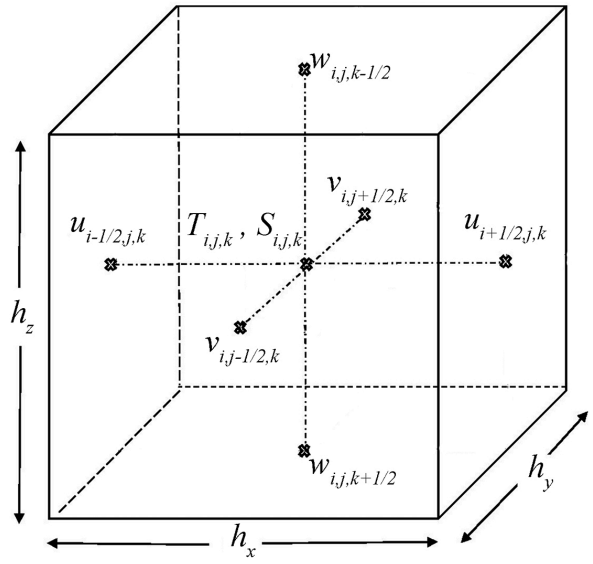


**F i g. 1.** Location of variables in the *C*-grid

The continuity equation (3) in discrete form at point $(i, j, k)$ is

$$\delta_x u_{i,j,k} + \delta_y v_{i,j,k} + \delta_z w_{i,j,k} = 0. \tag{7}$$

Write the differential in time $(q_{i,j,k} = q_{i,j,k}(t))$ and difference in space advection equation at the point $(i, j, k)$

$$\frac{dq_{i,j,k}}{dt} + \delta_x\left(u_{i,j,k}q_{i,j,k}\right) + \delta_y\left(v_{i,j,k}q_{i,j,k}\right) + \delta_z\left(w_{i,j,k}q_{i,j,k}\right) = 0, \tag{8}$$

where $q_{i+1/2,j,k}$, $q_{i,j+1/2,k}$, $q_{i,j,k+1/2}$ are not yet determined. Taking into account the notations of Eq. (6) and the discrete continuity Eq. (7), let us rewrite Eq. (8) in the form:

$$\begin{aligned}\frac{dq_{i,j,k}}{dt} + \left[u_{i+1/2,j,k}\left(q_{i+1/2,j,k} - q_{i,j,k}\right) - u_{i-1/2,j,k}\left(q_{i-1/2,j,k} - q_{i,j,k}\right)\right]h_x^{-1} + \\ + \left[v_{i,j+1/2,k}\left(q_{i,j+1/2,k} - q_{i,j,k}\right) - v_{i,j-1/2,k}\left(q_{i,j-1/2,k} - q_{i,j,k}\right)\right]h_y^{-1} + \\ + \left[w_{i,j,k+1/2}\left(q_{i,j,k+1/2} - q_{i,j,k}\right) - w_{i,j,k-1/2}\left(q_{i,j,k-1/2} - q_{i,j,k}\right)\right]\left(h_z^k\right)^{-1} = 0.\end{aligned} \tag{9}$$

Let the functional $Q$ and its derivative be written as follows:

$$Q_{i,j,k} = Q\left(q_{i,j,k}\right), \quad \frac{dQ_{i,j,k}}{dt} = Q'_{i,j,k}\frac{dq_{i,j,k}}{dt}, \quad \text{where} \quad Q'_{i,j,k} = \frac{dQ_{i,j,k}}{dq_{i,j,k}}. \tag{10}$$

Multiply Eq. (9) by $Q'_{i,j,k}$ and the result is transformed taking into account the continuity equation Eq. (7). Then we obtain the equation for $Q_{i,j,k}$:

$$\frac{dQ_{i,j,k}}{dt} + \{u_{i+1/2,j,k}[Q_{i,j,k} + Q'_{i,j,k}(q_{i+1/2,j,k} - q_{i,j,k})] - \\ -u_{i-1/2,j,k}[Q_{i,j,k} - Q'_{i,j,k}(q_{i,j,k} - q_{i-1/2,j,k})]\}h_x^{-1} + \\ +\{v_{i,j+1/2,k}[Q_{i,j,k} + Q'_{i,j,k}(q_{i,j+1/2,k} - q_{i,j,k})] - \\ -v_{i,j-1/2,k}[Q_{i,j,k} - Q'_{i,j,k}(q_{i,j,k} - q_{i,j-1/2,k})]\}h_y^{-1} + \\ +\{w_{i,j,k+1/2}[Q_{i,j,k} + Q'_{i,j,k}(q_{i,j,k+1/2} - q_{i,j,k})] - \\ -w_{i,j,k-1/2}[Q_{i,j,k} - Q'_{i,j,k}(q_{i,j,k} - q_{i,j,k-1/2})]\}(h_z^k)^{-1} = 0. \quad (11)$$

We require that $Q_{i,j,k}$ satisfies the advection equation, then its discrete form is

$$\frac{dQ_{i,j,k}}{dt} + [(Q_{i+1/2,j,k} - Q_{i,j,k})u_{i+1/2,j,k} - (Q_{i-1/2,j,k} - Q_{i,j,k})u_{i-1/2,j,k}]h_x^{-1} + \\ +[(Q_{i,j+1/2,k} - Q_{i,j,k})v_{i,j+1/2,k} - (Q_{i,j-1/2,k} - Q_{i,j,k})v_{i,j-1/2,k}]h_y^{-1} + \\ +[(Q_{i,j,k+1/2} - Q_{i,j,k})w_{i,j,k+1/2} - (Q_{i,j,k-1/2} - Q_{i,j,k})w_{i,j,k-1/2}](h_z^k)^{-1} + \\ +Q_{i,j,k}(\delta_x u_{i,j,k} + \delta_y v_{i,j,k} + \delta_z w_{i,j,k}) = 0. \quad (12)$$

The divergent form of nonlinear terms in (12) follows from relations

$$Q_{i,j,k} + Q'_{i,j,k}(q_{i+1/2,j,k} - q_{i,j,k}) = Q_{i+1,j,k} - Q'_{i+1,j,k}(q_{i+1,j,k} - q_{i+1/2,j,k}),$$
$$Q_{i,j,k} + Q'_{i,j,k}(q_{i,j+1/2,k} - q_{i,j,k}) = Q_{i,j+1,k} - Q'_{i,j+1,k}(q_{i,j+1,k} - q_{i,j+1/2,k}),$$
$$Q_{i,j,k} + Q'_{i,j,k}(q_{i,j,k+1/2} - q_{i,j,k}) = Q_{i,j,k+1} - Q'_{i,j,k+1}(q_{i,j,k+1} - q_{i,j,k+1/2}).$$

Then we obtain an expression for $q_{i+1/2,j,k}$ (the same way for $q_{i,j+1/2,k}$ and $q_{i,j,k+1/2}$):

$$q_{i+1/2,j,k} = \frac{(Q'_{i+1,j,k}q_{i+1,j,k} - Q_{i+1,j,k}) - (Q'_{i,j,k}q_{i,j,k} - Q_{i,j,k})}{Q'_{i+1,j,k} - Q'_{i,j,k}}. \quad (13)$$

The divergent form of $Q_{i,j,k}$ follows from Eqs. (11), (12). Taking into account relations in Eq. (10), the $Q_{i+1/2,j,k}$ has the next form (the same way for $Q_{i,j+1/2,k}$ and $Q_{i,j,k+1/2}$):

$$Q_{i+1/2,j,k} = q_{i+1/2,j,k}\frac{Q'_{i+1,j,k} + Q'_{i,j,k}}{2} - \frac{Q'_{i+1,j,k}q_{i+1,j,k} + Q'_{i,j,k}q_{i,j,k}}{2} + \\ + \frac{Q_{i+1,j,k} + Q_{i,j,k}}{2} = q_{i+1/2,j,k}\overline{Q'_{i+1/2,j,k}}^{x} - \overline{q_{i+1/2,j,k}Q'_{i+1/2,j,k}}^{x} + \overline{Q_{i+1/2,j,k}}^{x}. \quad (14)$$

Expressions (13) and (14) ensure that conservation laws are satisfied:

$$\left\{\frac{dq_{i,j,k}}{dt}\right\}^V = 0, \qquad \left\{\frac{dQ_{i,j,k}}{dt}\right\}^V = 0.$$

The obtained result can be easily generalized to the case of $R$ invariants $q^r_{i,j,k}$ ($r$ = 1, …, $R$) [13, 14].

Let us consider the case of two variables when $Q_{i,j,k} = Q(q^1_{i,j,k}, q^2_{i,j,k})$. Assume that $q^1_{i,j,k}$ and $q^2_{i,j,k}$ satisfy Eq. (8). Let the advection equation for $Q$ be written in the form where $Q_{i+1/2,j,k}$, $Q_{i,j+1/2,k}$, $Q_{i,j,k+1/2}$ are unknowns

$$\frac{dQ_{i,j,k}}{dt} + \delta_x\left(u_{i,j,k}Q_{i,j,k}\right) + \delta_y\left(v_{i,j,k}Q_{i,j,k}\right) + \delta_z\left(w_{i,j,k}Q_{i,j,k}\right) = 0. \qquad (15)$$

Assume that

$$\frac{dQ_{i,j,k}}{dt} = \left(Q_{i,j,k}\right)'_{q^1_{i,j,k}} \frac{dq^1_{i,j,k}}{dt} + \left(Q_{i,j,k}\right)'_{q^2_{i,j,k}} \frac{dq^2_{i,j,k}}{dt},$$

where $\left(Q_{i,j,k}\right)'_{q^1_{i,j,k}} = \dfrac{\partial Q_{i,j,k}}{\partial q^1_{i,j,k}}$, $\left(Q_{i,j,k}\right)'_{q^2_{i,j,k}} = \dfrac{\partial Q_{i,j,k}}{\partial q^2_{i,j,k}}$.

Carrying out appropriate transformations, taking into account the continuity equation Eq. (8) and the requirements of the divergence form of Eq. (15), we obtain the relation for $Q_{i+1/2,j,k}$ (the same way for $Q_{i,j+1/2,k}$ and $Q_{i,j,k+1/2}$):

$$\begin{aligned} Q_{i+1/2,j,k} = q^1_{i+1/2,j,k} \frac{\left(Q_{i+1,j,k}\right)'_{q^1_{i+1,j,k}} + \left(Q_{i,j,k}\right)'_{q^1_{i,j,k}}}{2} - \\ - \frac{\left(Q_{i+1,j,k}\right)'_{q^1_{i+1,j,k}} q^1_{i+1,j,k} + \left(Q_{i,j,k}\right)'_{q^1_{i,j,k}} q^1_{i,j,k}}{2} + \\ + q^2_{i+1/2,j,k} \frac{\left(Q_{i+1,j,k}\right)'_{q^2_{i+1,j,k}} + \left(Q_{i,j,k}\right)'_{q^2_{i,j,k}}}{2} - \\ - \frac{\left(Q_{i+1,j,k}\right)'_{q^2_{i+1,j,k}} q^2_{i+1,j,k} + \left(Q_{i,j,k}\right)'_{q^2_{i,j,k}} q^2_{i,j,k}}{2} + \frac{Q_{i+1,j,k} + Q_{i,j,k}}{2}. \end{aligned} \qquad (16)$$

The divergence form of Eq. (15) is provided by approximating $Q_{i,j,k}$ on the cell edges as Eq. (16).

Let $Q$ depend on $R$ functions $q^r_{i,j,k}$ ($r$ = 1, …, $R$, here $R$ is an integer):

$$Q_{i,j,k} = Q\left(q^1_{i,j,k}, q^2_{i,j,k}, \ldots, q^R_{i,j,k}\right).$$

Suppose that for each $r$ the following holds:

$$\left(Q_{i,j,k}\right)'_{q^r_{i,j,k}} = \frac{\partial Q_{i,j,k}}{\partial q^r_{i,j,k}}, \qquad \frac{dQ_{i,j,k}}{dt} = \sum_{r=1}^{R}\left[\left(Q_{i,j,k}\right)'_{q^r_{i,j,k}} \frac{dq^r_{i,j,k}}{dt}\right],$$

and these derivatives are limited. We also assume that for any $r$ the function $q^r_{i,j,k}$ satisfies the advection equation

$$\frac{dq^r_{i,j,k}}{dt} + \delta_x\left(u_{i,j,k}q^r_{i,j,k}\right) + \delta_y\left(v_{i,j,k}q^r_{i,j,k}\right) + \delta_z\left(w_{i,j,k}q^r_{i,j,k}\right) = 0. \qquad (17)$$

Having carried out the corresponding transformations, we obtain for any Eq. (17)

$$\frac{dq^r_{i,j,k}}{dt} + \left[u_{i+1/2,j,k}\left(q^r_{i+1/2,j,k} - q^r_{i,j,k}\right) - u_{i-1/2,j,k}\left(q^r_{i-1/2,j,k} - q^r_{i,j,k}\right)\right]h_x^{-1} +$$
$$+\left[v_{i,j+1/2,k}\left(q^r_{i,j+1/2,k} - q^r_{i,j,k}\right) - v_{i,j-1/2,k}\left(q^r_{i,j-1/2,k} - q^r_{i,j,k}\right)\right]h_y^{-1} +$$
$$+\left[w_{i,j,k+1/2}\left(q^r_{i,j,k+1/2} - q^r_{i,j,k}\right) - w_{i,j,k-1/2}\left(q^r_{i,j,k-1/2} - q^r_{i,j,k}\right)\right]\left(h_z^k\right)^{-1} = 0. \quad (18)$$

Multiplying each Eq. (18) by the corresponding $\left(Q_{i,j,k}\right)'_{q^r_{i,j,k}}$, Eq. (7) by $Q_{i,j,k}$ and summing the result, we get

$$\frac{dQ_{i,j,k}}{dt} + u_{i+1/2,j,k}\left[Q_{i,j,k} + \sum_{r=1}^{R}\left(Q_{i,j,k}\right)'_{q^r_{i,j,k}}\left(q^r_{i+1/2,j,k} - q^r_{i,j,k}\right)\right]h_x^{-1} -$$
$$-u_{i-1/2,j,k}\left[Q_{i,j,k} - \sum_{r=1}^{R}\left(Q_{i,j,k}\right)'_{q^r_{i,j,k}}\left(q^r_{i,j,k} - q^r_{i-1/2,j,k}\right)\right]h_x^{-1} +$$
$$+v_{i,j+1/2,k}\left[Q_{i,j,k} + \sum_{r=1}^{R}\left(Q_{i,j,k}\right)'_{q^r_{i,j,k}}\left(q^r_{i,j+1/2,k} - q^r_{i,j,k}\right)\right]h_y^{-1} -$$
$$-v_{i,j-1/2,k}\left[Q_{i,j,k} - \sum_{r=1}^{R}\left(Q_{i,j,k}\right)'_{q^r_{i,j,k}}\left(q^r_{i,j,k} - q^r_{i,j-1/2,k}\right)\right]h_y^{-1} +$$
$$+w_{i,j,k+1/2}\left[Q_{i,j,k} + \sum_{r=1}^{R}\left(Q_{i,j,k}\right)'_{q^r_{i,j,k}}\left(q^r_{i,j,k+1/2} - q^r_{i,j,k}\right)\right]\left(h_z^k\right)^{-1} -$$
$$-w_{i,j,k-1/2}\left[Q_{i,j,k} - \sum_{r=1}^{R}\left(Q_{i,j,k}\right)'_{q^r_{i,j,k}}\left(q^r_{i,j,k} - q^r_{i,j,k-1/2}\right)\right]\left(h_z^k\right)^{-1} = 0.$$

Assume that the functional $Q_{i,j,k}$ satisfies Eq. (15). Then we obtain recurrence relations for $Q$ on the cell edges $(i+1/2, j, k)$, $(i, j+1/2, k)$, $(i, j, k+1/2)$:

$$Q_{i+1/2,j,k} = \sum_{r=1}^{R}\left[q^r_{i+1/2,j,k}\frac{\left(Q_{i+1,j,k}\right)'_{q^r_{i+1,j,k}} + \left(Q_{i,j,k}\right)'_{q^r_{i,j,k}}}{2} -\right.$$

$$-\frac{\left(Q_{i+1,j,k}\right)'_{q^r_{i+1,j,k}} q^r_{i+1,j,k} + \left(Q_{i,j,k}\right)'_{q^r_{i,j,k}} q^r_{i,j,k}}{2}\Bigg] + \frac{Q_{i+1,j,k} + Q_{i,j,k}}{2},$$

$$Q_{i,j+1/2,k} = \sum_{r=1}^{R}\Bigg[q^r_{i,j+1/2,k}\frac{\left(Q_{i,j+1,k}\right)'_{q^r_{i,j+1,k}} + \left(Q_{i,j,k}\right)'_{q^r_{i,j,k}}}{2} -$$

$$-\frac{\left(Q_{i,j+1,k}\right)'_{q^r_{i,j+1,k}} q^r_{i,j+1,k} + \left(Q_{i,j,k}\right)'_{q^r_{i,j,k}} q^r_{i,j,k}}{2}\Bigg] + \frac{Q_{i,j+1,k} + Q_{i,j,k}}{2}, \qquad (19)$$

$$Q_{i,j,k+1/2} = \sum_{r=1}^{R}\Bigg[q^r_{i,j,k+1/2}\frac{\left(Q_{i,j,k+1}\right)'_{q^r_{i,j,k+1}} + \left(Q_{i,j,k}\right)'_{q^r_{i,j,k}}}{2} -$$

$$-\frac{\left(Q_{i,j,k+1}\right)'_{q^r_{i,j,k+1}} q^r_{i,j,k+1} + \left(Q_{i,j,k}\right)'_{q^r_{i,j,k}} q^r_{i,j,k}}{2}\Bigg] + \frac{Q_{i,j,k+1} + Q_{i,j,k}}{2}.$$

Eq. (19) can be interpreted as a finite-difference analogue of the functional $Q$ on the edges of cell ($i$, $j$, $k$) (Fig. 1). The advection equation for the functional $Q$ has the form of Eq. (15) and thus the zero equality of the volume integral of $dQ/dt$ is ensured. The obtained property corresponds to the conservation laws (5) with accuracy up to the time approximation. For each $r$ = 1, ..., $R$ we have

$$\left\{\frac{dq^r_{i,j,k}}{dt}\right\}^V = 0 \quad \text{and} \quad \left\{\frac{dQ\left(q^1_{i,j,k}, \ldots, q^R_{i,j,k}\right)}{dt}\right\}^V = 0.$$

An important feature of the obtained approximations in Eqs. (19) is that the $Q$ is an invariant for any $q^r_{i+1/2,j,k}$, $q^r_{i,j+1/2,k}$, $q^r_{i,j,k+1/2}$.

**Discrete state equation**

As an example, let us consider the state equation at point ($i$, $j$, $k$) in the form of a polynomial

$$\rho_{i,j,k} = Q\left(T_{i,j,k}, S_{i,j,k}\right) = \sum_{m=0}^{M}\sum_{n=0}^{N} a_{mn}\, T^m_{i,j,k} S^n_{i,j,k}, \qquad (20)$$

where $T$ and $S$ are the temperature and salinity, $a_{mn}$ are the polynomial coefficients, $M$ and $N$ are maximum degrees of the polynomial for temperature and salinity, respectively, at the same time $M$, $N$ are not necessarily integers. Following Eq. (13), the temperature and salinity on the cell edges ($i$, $j$, $k$) must satisfy Eqs. (21) so that $T_{i,j,k}, T^K_{i,j,k}, S_{i,j,k}, S^L_{i,j,k}$ are conserved:

$$T_{i+1/2,j,k} = \frac{K-1}{K}\left(\frac{T^K_{i+1,j,k} - T^K_{i,j,k}}{T^{K-1}_{i+1,j,k} - T^{K-1}_{i,j,k}}\right), \qquad (21a)$$

$$T_{i,j+1/2,k} = \frac{K-1}{K}\left(\frac{T^K_{i,j+1,k} - T^K_{i,j,k}}{T^{K-1}_{i,j+1,k} - T^{K-1}_{i,j,k}}\right), \qquad T_{i,j,k+1/2} = \frac{K-1}{K}\left(\frac{T^K_{i,j,k+1} - T^K_{i,j,k}}{T^{K-1}_{i,j,k+1} - T^{K-1}_{i,j,k}}\right).$$

$$S_{i+1/2,j,k} = \frac{L-1}{L}\left(\frac{S^L_{i+1,j,k} - S^L_{i,j,k}}{S^{L-1}_{i+1,j,k} - S^{L-1}_{i,j,k}}\right), \qquad (21b)$$

$$S_{i,j+1/2,k} = \frac{L-1}{L}\left(\frac{S^L_{i,j+1,k} - S^L_{i,j,k}}{S^{L-1}_{i,j+1,k} - S^{L-1}_{i,j,k}}\right), \qquad S_{i,j,k+1/2} = \frac{L-1}{L}\left(\frac{S^L_{i,j,k+1} - S^L_{i,j,k}}{S^{L-1}_{i,j,k+1} - S^{L-1}_{i,j,k}}\right).$$

The Eqs. (21) have a peculiarity if temperature or salinity are close to each other in neighboring points. This is especially important when the convective mixing procedure is used and then the temperature and salinity are equalized in neighboring horizons. To overcome this difficulty, Eqs. (21) are transformed to the following form (the same way for *j*, *k*):

$$T_{i+1/2,j,k} = \frac{K-1}{K}\left(T_{i,j,k} + \frac{T^{K-1}_{i+1,j,k}}{\Phi\left(T_{i+1,j,}, T_{i,j,k}\right)}\right),$$
$$S_{i+1/2,j,k} = \frac{L-1}{L}\left(S_{i,j,k} + \frac{S^{L-1}_{i+1,j,k}}{\Psi(S_{i+1,j,k}, S_{i,j,k})}\right), \qquad (22)$$

where

$$\Phi\left(T_{i+1,j,k},\ T_{i,j,k}\right) = \sum_{m=0}^{K-2} T^{K-m-2}_{i+1,j,k} T^m_{i,j,k}\,, \Psi\left(S_{i+1,j,k},\ S_{i,j,k}\right) = \sum_{n=0}^{L-2} S^{L-n-2}_{i+1,j,k} S^n_{i,j,k}.$$

The divergence form of the discrete density advection equation follows from Eqs. (20) in which $\rho_{i+1/2,j,k}, \rho_{i,j+1/2,k}, \rho_{i,j,k+1/2}$ are in the form:

$$\rho_{i+1/2,j,k} =$$
$$= \frac{K-1}{K}\frac{T^K_{i+1,j,k} - T^K_{i,j,k}}{T^{K-1}_{i+1,j,k} - T^{K-1}_{i,j,k}} \sum_{m=1}^{M}\sum_{n=0}^{N} a_{mn} m \overline{T^{m-1}_{i+1/2,j,k} S^n_{i+1/2,j,k}}^{x} +$$
$$+ \frac{L-1}{L}\frac{S^L_{i+1,j,k} - S^L_{i,j,k}}{S^{L-1}_{i+1,j,k} - S^{L-1}_{i,j,k}} \sum_{m=0}^{M}\sum_{n=1}^{N} a_{mn}\, n \overline{T^m_{i+1/2,j,k} S^{n-1}_{i+1/2,j,k}}^{x} -$$
$$- \sum_{m=1}^{M}\sum_{n=0}^{N} a_{mn} m \overline{T^m_{i+1/2,j,k} S^n_{i+1/2,j,k}}^{x} - \sum_{m=0}^{M}\sum_{n=1}^{N} a_{mn} \overline{n T^m_{i+1/2,j,k} S^n_{i+1/2,j,k}}^{x} +$$
$$+ \sum_{m=0}^{M}\sum_{n=0}^{N} a_{mn} \overline{T^m_{i+1/2,j,k} S^n_{i+1/2,j,k}}^{x},$$

$$\rho_{i,j+1/2,k} =$$
$$= \frac{K-1}{K}\frac{T^K_{i,j+1,k}-T^K_{i,j,k}}{T^{K-1}_{i,j+1,k}-T^{K-1}_{i,j,k}}\sum_{m=1}^{M}\sum_{n=0}^{N} a_{mn} m \overline{T^{m-1}_{i,j+1/2,k} S^n_{i,j+1/2,k}}^{y} +$$
$$+ \frac{L-1}{L}\frac{S^L_{i,j+1,k}-S^L_{i,j,k}}{S^{L-1}_{i,j+1,k}-S^{L-1}_{i,j,k}}\sum_{m=0}^{M}\sum_{n=1}^{N} a_{mn} n \overline{T^m_{i,j+1/2,k} S^{n-1}_{i,j+1/2,k}}^{y} -$$
$$- \sum_{m=1}^{M}\sum_{n=0}^{N} a_{mn} m \overline{T^m_{i,j+1/2,k} S^n_{i,j+1/2,k}}^{y} - \sum_{m=0}^{M}\sum_{n=1}^{N} a_{mn} n \overline{T^m_{i,j+1/2,k} S^n_{i,j+1/2,k}}^{y} +$$
$$+ \sum_{m=0}^{M}\sum_{n=0}^{N} a_{mn} \overline{T^m_{i,j+1/2,k} S^n_{i,j+1/2,k}}^{y}, \qquad (23)$$
$$\rho_{i,j,k+1/2} =$$
$$= \frac{K-1}{K}\frac{T^K_{i,j,k+1}-T^K_{i,j,k}}{T^{K-1}_{i,j,k+1}-T^{K-1}_{i,j,k}}\sum_{m=1}^{M}\sum_{n=0}^{N} a_{mn} m \overline{T^{m-1}_{i,j,k+1/2} S^n_{i,j,k+1/2}}^{z} +$$
$$+ \frac{L-1}{L}\frac{S^L_{i,j,k+1}-S^L_{i,j,k}}{S^{L-1}_{i,j,k+1}-S^{L-1}_{i,j,k}}\sum_{m=0}^{M}\sum_{n=1}^{N} a_{mn} n \overline{T^m_{i,j,k+1/2} S^{n-1}_{i,j,k+1/2}}^{z} -$$
$$- \sum_{m=1}^{M}\sum_{n=0}^{N} a_{mn} m \overline{T^m_{i,j,k+1/2} S^n_{i,j,k+1/2}}^{z} - \sum_{m=0}^{M}\sum_{n=1}^{N} a_{mn} n \overline{T^m_{i,j,k+1/2} S^n_{i,j,k+1/2}}^{z} +$$
$$+ \sum_{m=0}^{M}\sum_{n=0}^{N} a_{mn} \overline{T^m_{i,j,k+1/2} S^n_{i,j,k+1/2}}^{z}.$$

In contrast to [7, 8, 12], the approximations obtained in (21), (22) belong to the class of nonlinear approximations. Eqs. (21) and (22) ensure the conservation of $T_{i,j,k}$ and $T^K_{i,j,k}$, $S_{i,j,k}$ and $S^L_{i,j,k}$ when integrating over the whole domain. It is important to note that, as well as in the general case, the values of $K$, $L$, $M$, $N$ can be different in Eqs. (21), (22), and (23). Moreover, they may not be integers. Another important quality of the obtained approximations is their compactness. The conservation properties are achieved on a three-point template, which, according to the results of [12], is an essential advantage over schemes that apply an extended template. As a result, we obtain

$$\left\{\frac{dT_{i,j,k}}{dt}\right\}^V = 0,\ \left\{\frac{dT^K_{i,j,k}}{dt}\right\}^V = 0,\ \left\{\frac{dS_{i,j,k}}{dt}\right\}^V = 0,\ \left\{\frac{dS^L_{i,j,k}}{dt}\right\}^V = 0,\ \left\{\frac{d\rho_{i,j,k}}{dt}\right\}^V = 0.$$

At $R = 2$ and $q^1_{i,j,k} = T_{i,j,k}, q^2_{i,j,k} = S_{i,j,k}$ with a polynomial dependence of density on temperature and salinity, relations (19) lead to approximations (23), from which the required property follows $\left\{\frac{d\rho_{i,j,k}}{dt}\right\}^V = 0$.

## Testing new approximation for modelling the Black Sea circulation

### Model and data

The scheme (22), (23) was tested on the example of modelling the Black Sea circulation. Numerical experiments were carried out using an eddy-resolving model of Marine Hydrophysical Institute of Russian Academy of Sciences [23] and data from the atmospheric reanalysis ERA5 [1] for 2016. The MHI-model is based on the system of the primitive ocean equations under the Boussinesq and hydrostatics assumptions; the finite-difference analogue of the equations is implemented on the *C*-grid (Fig. 1). The vertical turbulent mixing is parameterized by the Mellor–Yamada closure model 2.5 [24]. The full problem formulation, initial and boundary conditions, assumptions and parameterizations used are presented in detail in the Appendix of [23]. The spatial resolution of the MHI-model is 1.64 km in horizontal coordinates, while non-uniform *z*-horizons with depths ranging from 2.5 m near the surface to 200 m near the bottom are defined in the vertical direction.

Scheme (22) was used in finite-difference analogues of the heat and salt advection-diffusion equations when integer values of the parameters $K$ and $L$ vary from 2 till 10. Validation of the preliminary numerical experiment results using data from *in-situ* measurements of temperature and salinity profiles [25] showed that the smallest modelling error of the Black Sea thermohaline fields was achieved using $K = 3$, $L = 5$, which corresponded to the discrete temperature advection equation conserving $T$, $T^3$, and the salinity advection equation conserving $S$, $S^5$. Substituting $K = L = 2$ in Eq. (22), the approximation of temperature and salinity on the cell edges was reduced to the traditional form (the same way for $i$, $j$):

$$T_{i,j,k+1/2} = \overline{T_{\iota,j,k+1/2}}^{z}, \qquad S_{i,j,k+1/2} = \overline{S_{\iota,j,k+1/2}}^{z}. \tag{24a}$$

For $K = 3$, $L = 5$ we get (the same way for $i$, $j$)

$$T_{i,j,k+1/2} = \frac{2}{3}\frac{T_{i,j,k+1}^2 + T_{i,j,k+1}T_{i,j,k} + T_{i,j,k}^2}{T_{i,j,k+1} + T_{i,j,k}}, \tag{24b}$$

$$S_{i,j,k+1/2} = \frac{4}{5}\frac{S_{i,j,k+1}^4 + S_{i,j,k+1}^3 S_{i,j,k} + S_{i,j,k+1}^2 S_{i,j,k}^2 + S_{i,j,k+1} S_{i,j,k}^3 + S_{i,j,k}^4}{S_{i,j,k+1}^3 + S_{i,j,k+1}^2 S_{i,j,k} + S_{i,j,k+1} S_{i,j,k}^2 + S_{i,j,k}^3}.$$

Seawater density in the MHI-model is calculated as second-degree polynomial of temperature and first-degree of salinity [26] and in accordance with the notations in Eq. (20) is written as:

$$\rho_{i,j,k} = \sum_{m=0}^{2}\sum_{n=0}^{1} a_{mn} T^m S^n = a_{00} + \alpha_{10} T_{i,j,k} + \\ + \alpha_{01} S_{i,j,k} + \alpha_{20} T_{i,j,k}^2 + \alpha_{11} S_{i,j,k} T_{i,j,k}. \tag{25}$$

[1] Copernicus, 2023. *Copernicus Climate Change Service, Climate Data Store. ERA5 Hourly Data on Single Levels from 1940 to Present*. [online] Available at: https://cds.climate.copernicus.eu/datasets/reanalysis-era5-single-levels?tab=overview https://doi.org/10.24381/cds.adbb2d47 [Accessed: 25 January 2026].

We assume $a_{21} = 0$ in Eq. (25).

For the same representation of the buoyancy work in the equations rate of change of kinetic and potential energy, the density on the cell edges (Fig. 1) must satisfy Eqs. (23) with $K = L = 2$, $M = 2$, $N = 1$ for the first experiment and $K = 3$, $L = 5$, $M = 2$, $N = 1$ for the second one. To evaluate the effect of the two conservation schemes directly on the simulation results, we restricted ourselves to representing the density on the cell edges as (for $K = L = 2$, $M = 2$, $N = 1$)

$$\rho_{i,j,k+1/2} = \alpha_{10}\overline{T_{i,j,k+1/2}}^{z} + \alpha_{01}\overline{S_{i,j,k+1/2}}^{z} + \alpha_{20}T_{i,j,k+1}T_{i,j,k} + \\ +\alpha_{11}\frac{T_{i,j,k}S_{i,j,k+1} + T_{i,j,k+1}S_{i,j,k}}{2}.$$

The peculiarities of the reconstructed hydrophysical fields when changing the approximation scheme of advective heat and salt transport were considered comparing the Black Sea circulation modelling results from 2016 for the cases $K = L = 2$ (experiment T2S2 with Eqs. (24a)) and $K = 3$, $L = 5$ (experiment T3S5 with Eqs. (24b)). Both runs were carried out for a period of one year without assimilation of observational data. The outputs were daily fields of temperature, salinity, and current velocity. *In-situ* temperature and salinity obtained by Argo floats [2] and by cruises of the R/V *Professor Vodyanitsky* [27] in 2016 were used to validate the modelling results.

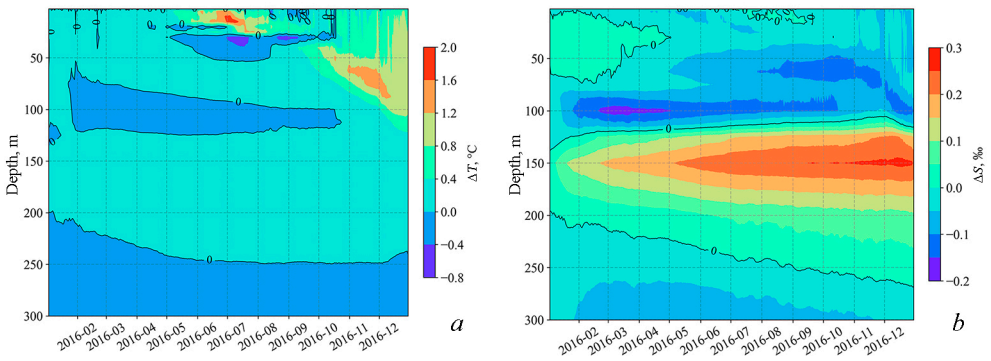


**F i g. 2.** Variations with depth and time for $\Delta T$ (*a*) and $\Delta S$ (*b*)

## Comparison of the hydrophysical fields

Fig. 2 shows a diagram of the variation with depth and time of the difference between daily temperature and salinity calculated in the T2S2 and T3S5 experiments:

$$\Delta T(z,t) = \langle T_{\mathrm{T2S2}}\rangle^{z} - \langle T_{\mathrm{T3S5}}\rangle^{z}, \quad \Delta S(z,t) = \langle S_{\mathrm{T2S2}}\rangle^{z} - \langle S_{\mathrm{T3S5}}\rangle^{z},$$

[2] Argo, 2026. *Argo Float Data and Metadata from Global Data Assembly Centre (Argo GDAC)* [dataset]. SEANOE. https://doi.org/10.17882/42182

where $<>^z$ is the average over $z$-layer area. As can be seen from Fig. 2, *a*, the largest modulus differences between the temperature fields were observed in summer in the thermocline layer at 15–30 m depths. The zone of large positive values of $\Delta T$ indicates that the temperature in the T2S2 experiment was higher than in T3S5 for the 5–15 m layer. Large values were also observed in November–December at 50–100 m depths. In June–August in the 25–50 m layer, the temperature in the T2S2 experiment was lower than in the T3S5. The maximum difference between the salinity fields in the two runs was found in the permanent halocline layer at 100–150 m depths, starting from spring (Fig. 2, *b*). As can be seen during the year, the salinity was higher in the 50–100 m layer and lower in the 125–200 m layer in the T3S5 experiment than in the T2S2 data. Moreover, $\Delta S$ increased toward the end of the year reaching a maximum in December at 150 m horizon.

Comparison of the model fields with temperature and salinity measurements obtained by Argo floats (Table 1 and Tables 1–4 in [25]) showed that in the T3S5 experiment the modelling error of salinity decreased in the upper 100-meter layer, while the modelling error of temperature changes little in the upper 30-meter layer and decreases below 30 m. Below 300 m, the RMSE of temperature and salinity differed little in the two experiments. Thus, the data of Fig. 2 and Table demonstrate that in the T3S5 experiment, the salinity in the vicinity of the lower boundary of the permanent halocline and the temperature in the zone of the seasonal thermocline were reconstructed more accurately.

**RMSE temperature and salinity between *in-situ* and model data**

| Depth, m | $T^{T2S2}$, °C | $S^{T2S2}$, ‰ | $T^{T3S5}$, °C | $S^{T3S5}$, ‰ |
|---|---|---|---|---|
| 0–5 | 0.79 | 0.28 | 0.94 | 0.22 |
| 5–30 | 1.53 | 0.23 | 1.54 | 0.17 |
| 30–100 | 1.12 | 0.67 | 0.84 | 0.56 |
| 100–300 | 0.26 | 0.48 | 0.27 | 0.50 |
| 300–800 | 0.05 | 0.09 | 0.07 | 0.10 |
| 800–1500 | 0.03 | 0.08 | 0.03 | 0.08 |

Let us consider the spatial distributions of hydrodynamic characteristics during the period under study. At the beginning of the year, the difference between the experiment results was insignificant, which indicated the predominant influence of initial conditions. Further on, quantitative differences between the fields in the two experiments emerged. According to the diagram in Fig. 2, *a*, the maximum difference between the results of temperature calculations was reached in early July at 15 m horizon. Fig. 3 shows the temperature and current velocity fields for July 1, 2016.

As seen in Fig. 3, *a*, *b*, the temperature fields in the two experiments were qualitatively similar during summer: the increased temperature values were located near the western coast, the Crimean coast and the Anatolian coast, while lower temperatures occurred near the North Caucasus coast and on the Northwestern Shelf.

However, the water temperature near the western coast was higher, and the water area with temperatures of 21–23 °C in the southwestern deep-sea part was much larger in the T2S2 experiment than in the T3S5. Comparison of the velocity fields showed that in the T3S5 experiment the velocity and width of the Rim Current were larger in the southwestern sea (Fig. 3, *d*) and the upwelling velocity was larger in the region between 30°E and 32°E ($w < 0$, Fig. 3, *f*).

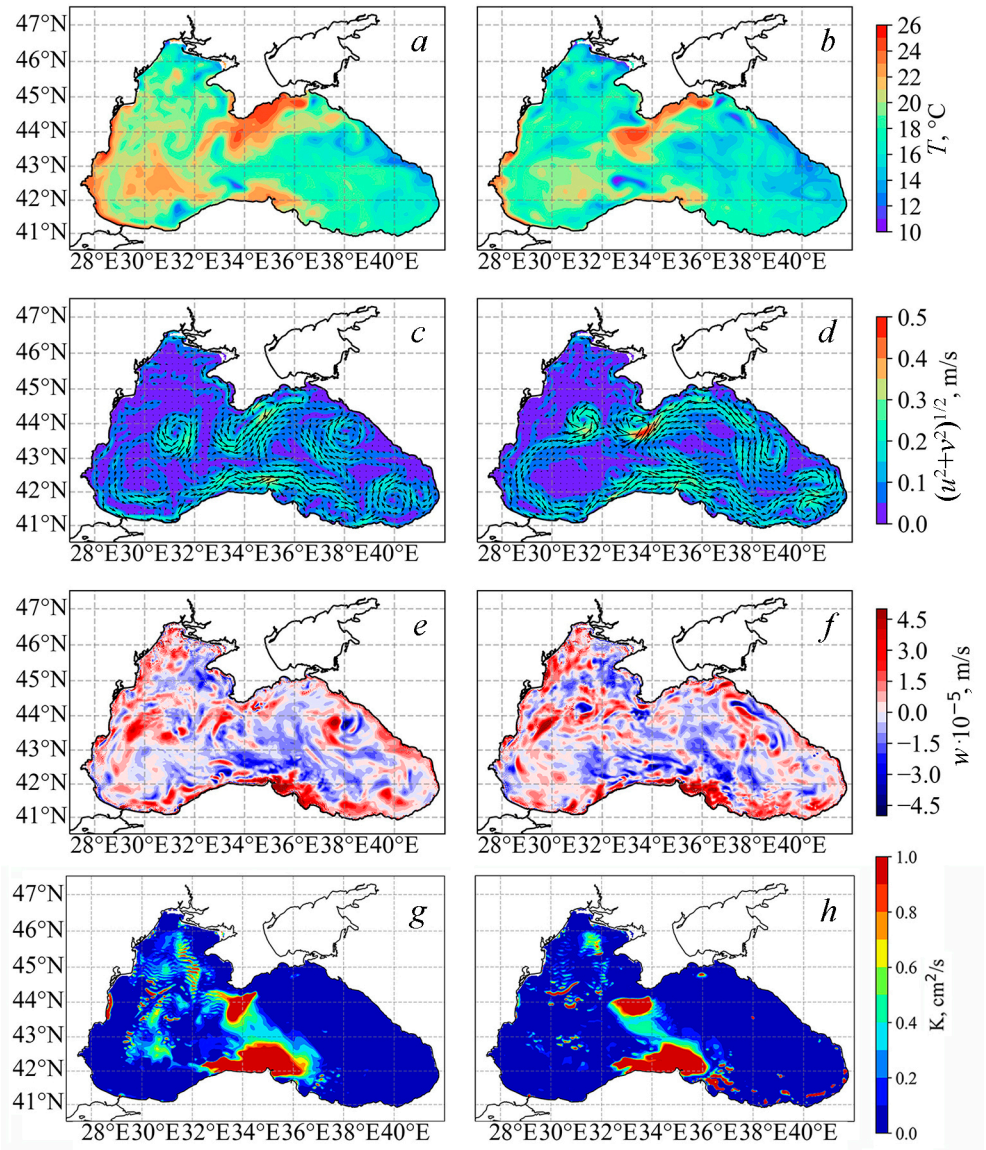


**F i g. 3.** Temperature fields (*a*, *b*) and horizontal velocity fields (*c*, *d*) at the 15 m horizon, vertical velocity (*e*, *f*) and vertical diffusion coefficient (*g*, *h*) at the 17.5 m horizon on July 1, 2016 from the results of experiments T2S2 (*a*, *c*, *e*, *g*) and T3S5 (*b*, *d*, *f*, *h*)

The analysis of the vertical turbulent diffusion coefficient maps demonstrated that the main mechanism responsible for the higher temperature values in the T2S2 experiment was the intense vertical turbulent exchange. In the southwestern part, the coefficient values in the T2S2 (Fig. 3, *g*) were about 3 times larger than those in the T3S5 (Fig. 3, *h*). Thus, the temperature in the T3S5 data was lower due to a decrease in the vertical diffusion of warm surface water and an increase in the upwelling velocity of cold deep water.

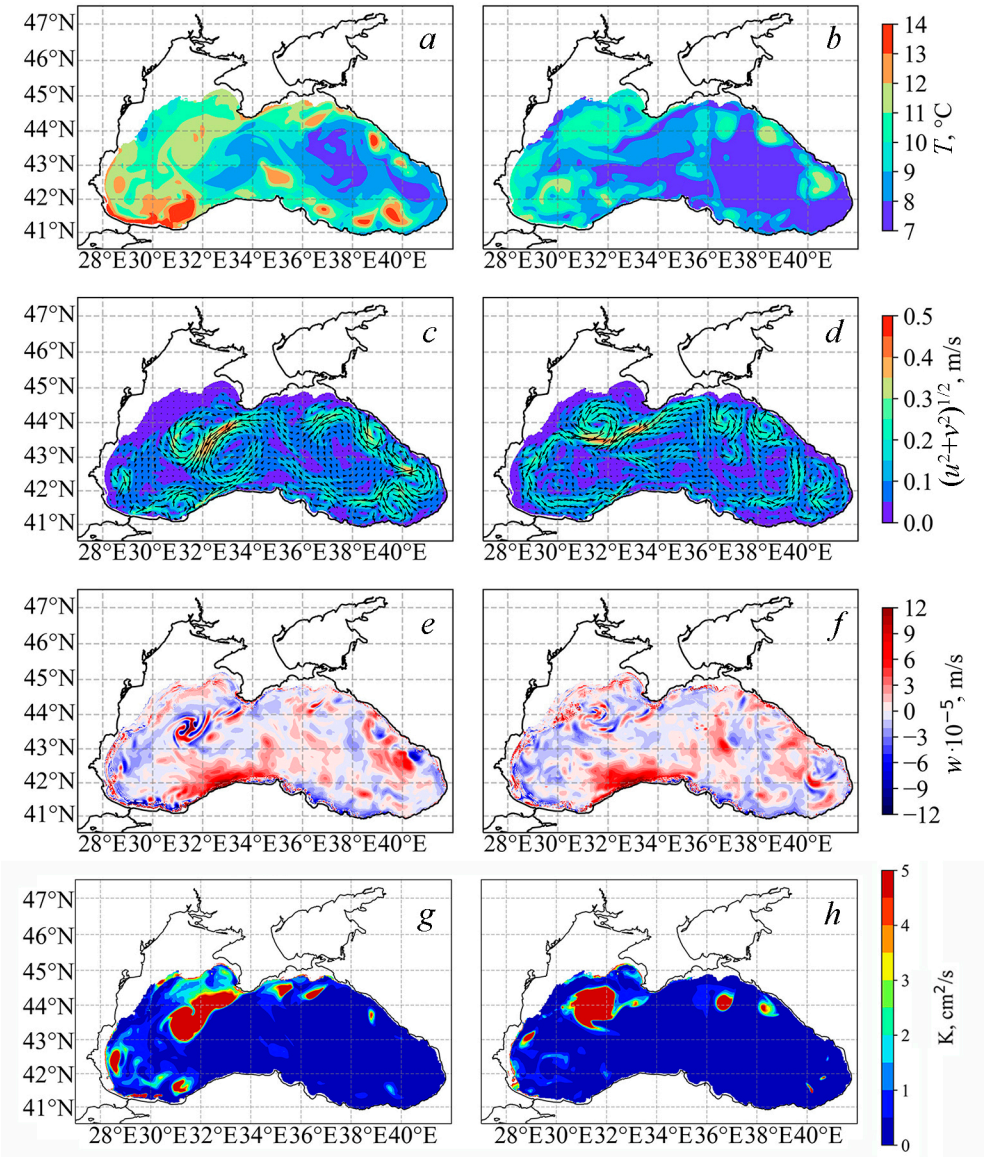


**F i g. 4.** Temperature fields (*a*, *b*) and horizontal velocity fields (*c*, *d*) at the 75 m horizon, vertical velocity (*e*, *f*) and vertical diffusion coefficient (*g*, *h*) at the 81.25 m horizon on December 1, 2016 from the results of experiments T2S2 (*a*, *c*, *e*, *g*) and T3S5 (*b*, *d*, *f*, *h*)

The difference in temperature near the Crimean coast was related to the differences in the Rim Current structure and the dynamics of mesoscale eddies. As can be seen from Fig. 3, *c*, *e*, the continuity of the Rim Current was broken in the T2S2 experiment, and mesoscale anticyclones developing in the northern sea part generated extensive domains with downwelling of warm surface water. In the T3S5 experiment, the Rim Current was pressed against the coast and the sizes of anticyclones were smaller (Fig. 3, *d*), so the warm water cores were more compact and located close to the shore.

In the second half of the year, the water temperature fields of the upper 30-meter layer were qualitatively similar, but the water temperature in the western part was higher in the T2S2 experiment. By the end of the year, the difference between the experiment results increased with the intensification of water cooling and vertical mixing processes. As noted in Fig. 2, *a*, in the cold season, the area-averaged temperature values in the T2S2 exceeded the T3S5 data at 50–100 m horizons. Fig. 4 presents the fields of temperature, current velocity components, and vertical diffusion coefficient on December 1, 2016.

As seen in Fig. 4 *a*, *b*, the largest temperature differences between experiments were observed at the basin periphery and in the southwestern sea. Coastal anticyclonic eddies near the Anatolian and Caucasus coasts were similar in size and intensity of current velocity (Fig. 4, *c–f*) in the two experiments, so the higher temperature anomalies in the T2S2 than in the T3S5 were related to the downwelling of warmer overlying waters.

In the southwestern sea part in the T2S2 experiment, the domain of waters with temperature of 14 °C (Fig. 4, *a*) was formed as a result of intensive vertical mixing (Fig. 4, *g*) in the zone of anticyclonic coastal eddies (Fig. 4, *c*). In the T3S5 experiment, the value of the diffusion coefficient was 3–4 times smaller in the same domain (Fig. 4, *h*). For both winter and summer seasons, the largest differences in the temperature and structure of the current field were localized in the western sea part. Also note the more regular character of the Rim Current in the T3S5 experiment, which is consistent with the observations [28].

The differences in the vertical structure of the temperature fields in summer were manifested in the thickness of the Cold Intermediate Layer (CIL; waters with temperatures less than 8 °C) and the structure of the thermocline. As can be seen from Fig. 5, *b*, in the T3S5 experiment the CIL was thinner, its structure was continuous, and the depth was decreased in the central sea part. But the depth and thickness of the thermocline were larger than in the T2S2. Comparison of vertical cross-sections shows that in August–September, the thickness of the thermocline in the T3S5 decreased, while the structure of the CIL was preserved.

By the beginning of winter, the temperature of the upper 50-meter layer in the T3S5 experiment was lower, and the CIL was partially destroyed, preserved only in the eastern deep-sea part (Fig. 5, *d*). Comparison of temperature cross-sections with vertical cross-sections of diffusion coefficient and vertical velocity shows that spatially the areas of the CIL destruction coincided with the zones with a frequent change in the vertical velocity sign in the meridional direction (frequent alternation of upwelling and downwelling).

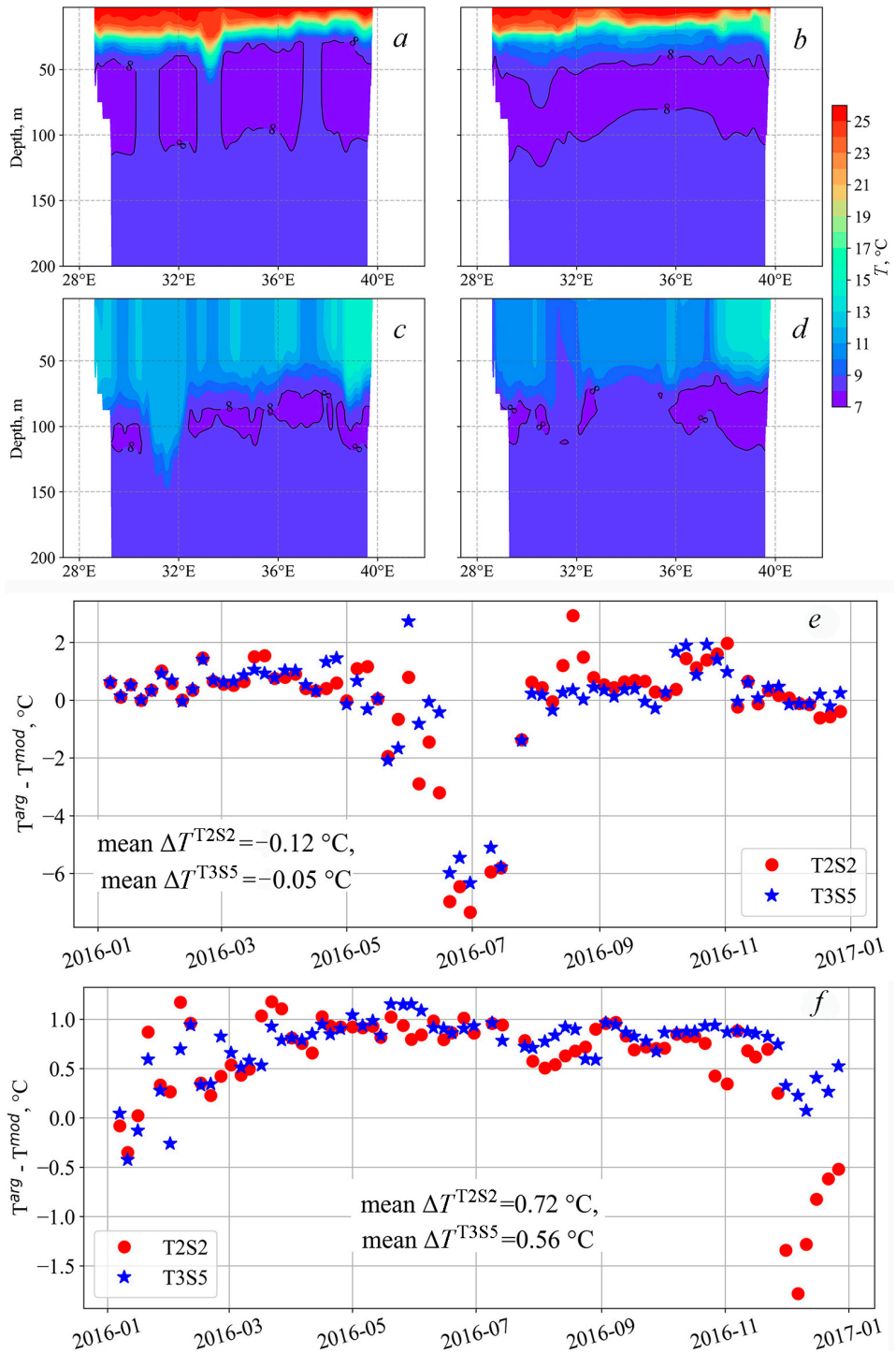


**F i g. 5.** Temperature cross-section along 43.5°N on July 1, 2016 (*a*, *b*) and on December 1, 2016 (*c*, *d*) from the results of experiments T2S2 (*a*, *c*) and T3S5 (*b*, *d*). Temperature deviation between Argo float #9601895 and model data at the 15 m horizon (*e*), between Argo float #9601832 and model data at the 75 m horizon (*f*)

Accuracy of the reconstructed temperature fields in the two experiments was assessed on the basis of comparison with the data of Argo floats. Fig. 5, *e* shows the deviation of the model temperature from the measurements by float #9601895, which profiled in the western sea part during 2016. As can be seen, the scatter of values in the thermocline layer in May–August was smaller in the T3S5 experiment, and the annual mean deviation decreases almost twice compared to the T2S2. The temperature overestimation ($T^{mod} > T^{arg}$) in early July (Fig. 5, *e*) was related to the influence of the atmosphere: both experiments showed an excess of the measured data by about 6 °C, which was due not to the properties of the approximation scheme but to the increase in the solar radiation flux. According to the data from float #9601832 (Fig. 5, *f*), which operated in the Rim Current zone near the Anatolian coast and the Caucasus, in both experiments the temperature values in the CIL were underestimated ($T^{mod} < T^{arg}$), while the mean deviation in the T3S5 experiment was smaller due to the more accurate reconstruction of the temperature in November–December 2016.

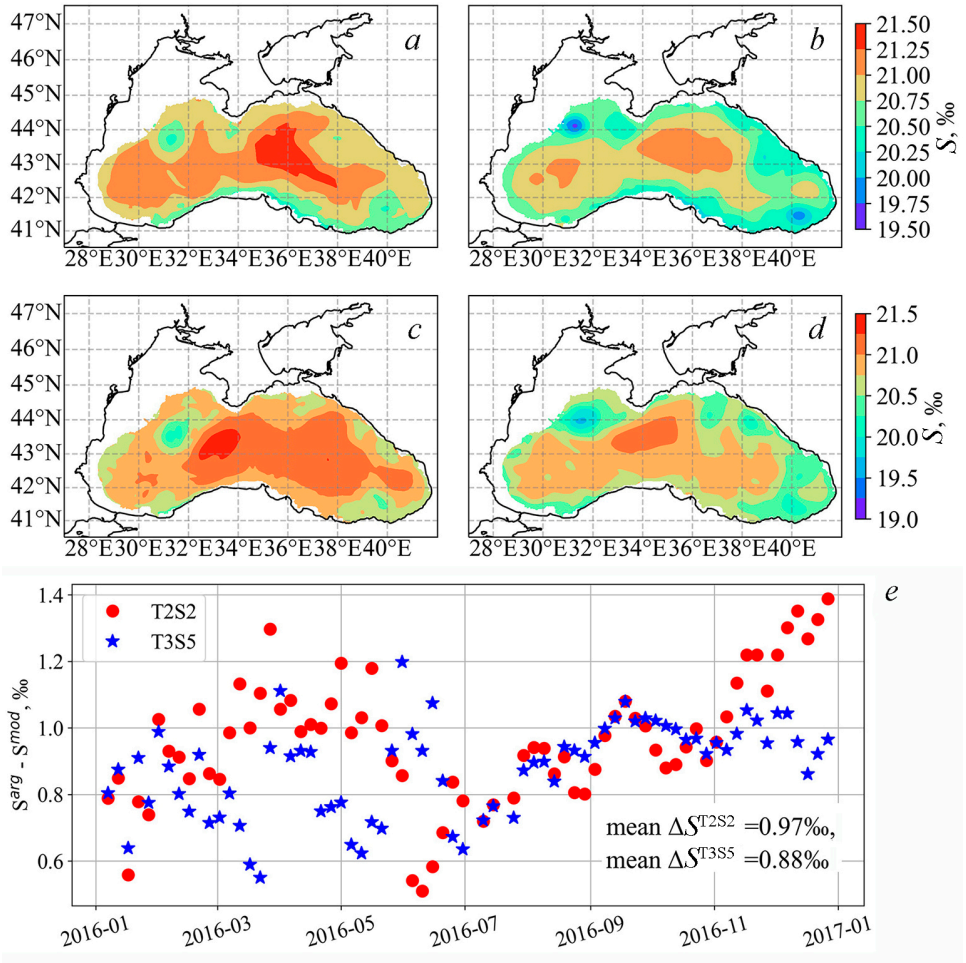


**F i g. 6.** Salinity fields on July 1, 2016 (*a*, *b*) and on December 1, 2016 (*c*, *d*) at the 150 m horizon from the results of experiments T2S2 (*a*, *c*) and T3S5 (*b*, *d*). Salinity deviation between Argo float #9601895 and model data at the 150 m horizon (e)

According to Fig. 2, *b*, the most significant differences in the salinity fields were manifested at the lower boundary of the permanent halocline and reached the highest values in the second half of the year. As can be seen from Fig. 6, *a*, *c* at 150 m horizon, the salinity in the central sea part was higher in the T2S2 experiment. At the same time, in the T3S5 experiment domains with salinity less than 20‰ were observed in the zone of mesoscale anticyclonic eddies (Fig. 6, *b*, *d*), which was consistent with observations. The lower salinity values in the eddies compared to the T2S2 experiment indicated the more intense anticyclonic rotation of the waters.

Also, in the T3S5 experiment the salinity in the southwestern and northeastern parts of the continental slope was lower by about 0.75‰ than in the T2S2, while in the central deep-sea part the salinity values were close (the difference is less than 0.25‰). Analysis of the annual mean salinity fields at the 150 m horizon showed that near the western boundary of the basin at latitude 43°N, the salinity gradient along the east longitude was 0.23 and 0.29‰ per degree for experiments T2S2 and T3S5, respectively. Consequently, in the T3S5 the horizontal salinity gradients between the periphery and the deep part were larger, and thus the velocities in the Rim Current were greater.

Comparison of the model results with salinity measurements in the Rim Current zone at the 150 m horizon (based on data from the Argo float #6901895) showed that in general the MHI-model gave lower salinity values compared to observations, but in the cold months of the year (January – April, November – December) the modelling error of salinity fields in the T3S5 experiment decreased (Fig. 6, *e*). The annual mean salinity deviation was also smaller in the T3S5 experiment.

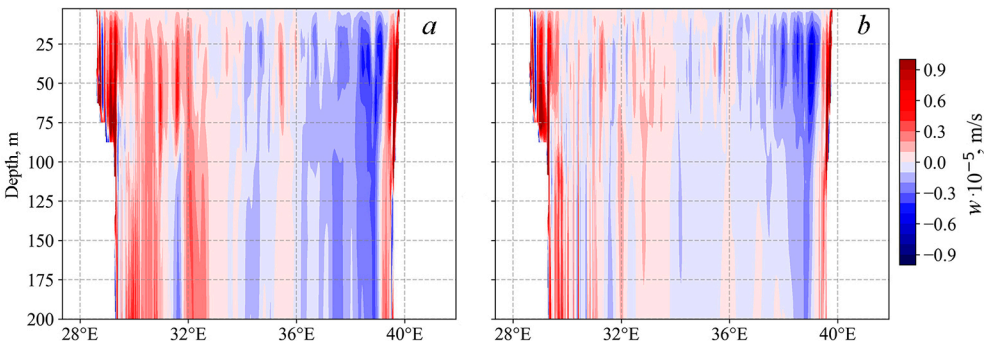


**F i g. 7.** Cross-section of annual mean vertical velocity along 43.5°N from the results of experiments T2S2 (*a*) and T3S5 (*b*)

Analysis of the vertical salinity profiles showed that, throughout the year, salinity in T3S5 was about 0.5‰ higher in the upper layer and lower in the 100–150 m layer compared to T2S2. Comparison of the salinity and vertical velocity fields indicated that this structure was due to the configuration of upwelling and downwelling zones. Fig. 7 shows the annual mean vertical velocity fields in the two experiments on a zonal cross-section along 43.5°N. As can be seen, in the T2S2 experiment between 30 and 32°E there was more intense downwelling in the upper 100-m layer ($w > 0$, Fig. 7, *a*), which corresponded to the anticyclonic water rotation and the inflow of less saline water from the overlying layers. In the central sea part, the domain was observed with saline deep-water upwelling with velocity higher than

in T3S5. Comparison of Fig. 7, a and *b* showed that at the basin periphery the downwelling velocities were close in magnitude for both experiments, and in the central sea part the upwelling and downwelling velocities were lower in the T3S5 experiment.

**Kinetic and available potential energy**

As the experimental results showed, changing the approximation scheme of the advective heat and salt transport operator reduced the modelling error in the thermohaline fields, which in turn affected the energy characteristics of the circulation through changes in the seawater density. Analyzing the circulation energetics permitted us to evaluate the redistribution of energy in the system as well as to compare the spectral properties of the model versions. The currents kinetic energy (*KE*) and available potential energy (*APE*) were calculated as follows:

$$KE = \rho_0 \frac{u^2 + v^2}{2}, \quad APE = g \frac{\left(\rho - \overline{\langle\rho\rangle^z}\right)^2}{2} \left(\frac{d\overline{\langle\rho\rangle^z}}{dz}\right)^{-1},$$

where $\overline{\langle\rho\rangle^z}$ is annual mean local density averaged over a *z*-layer area.

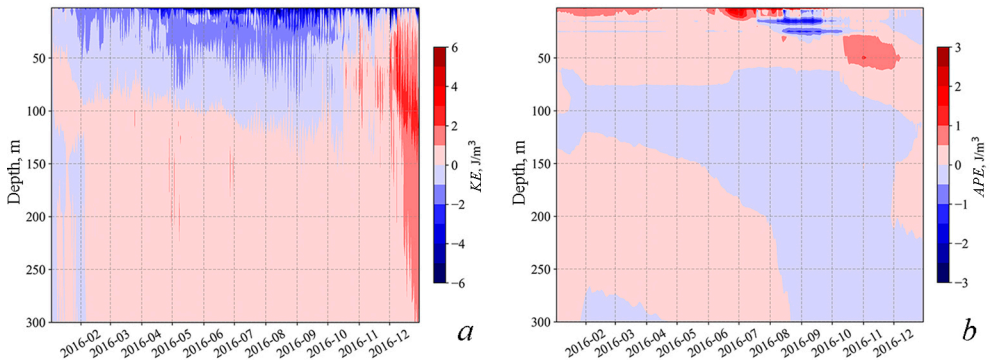


**F i g. 8.** Variations with depth and time for Δ*KE* (*a*) and Δ*APE* (*b*)

Fig. 8 shows the variation with time and depth of the difference between the layer-averaged *KE* and *APE* values in the two experiments $\Delta KE(z,t) = \langle KE_{\mathrm{T2S2}}\rangle^z - \langle KE_{\mathrm{T3S5}}\rangle^z$, $\Delta APE(z,t) = \langle APE_{\mathrm{T2S2}}\rangle^z - \langle APE_{\mathrm{T3S5}}\rangle^z$.

The mean *KE* was greater in the upper 75-m layer from February to October in the T3S5 experiment, the largest difference values having been observed at the 5-m horizon in summer. Since the boundary conditions in the experiments were the same, the increase in energy at the upper horizons was presumably due to a decrease in dissipation losses. Comparing Figs. 2 and 8, *a*, there was some correspondence between the increase in *KE* and the increase in temperature for the T3S5 experiment in the 25–50 m layer from May to September. Below 100 m, the mean *KE* was greater in the T2S2 experiment, but by the end of the year the currents were more intense in almost the entire layer with a maximum difference in December at 75–125 m horizons. The lower *KE* in the T3S5 below 100 m seemed to be related to the refinement of the salinity field in December 2016. As seen in Fig. 6, *e*,

the salinity modelling error increased at the end of the year to 1.4‰ in the T2S2 data, whereas in T3S5 the error magnitude was about 1‰.

Comparison of Figs. 2 and 8, *b* showed that the largest difference in the *APE* values was observed in June – September in the upper 30-meter layer. At the same time, increased values of *APE* corresponded to higher temperature in the T2S2, while decreased values corresponded to higher temperature in T3S5 (Fig. 2, *a*). Despite the fact that salinity plays a larger role in determining the density in the Black Sea [29], the relationship between *APE* and temperature is due to the increased contribution of temperature to seawater density during the warm season in the upper 30-meter layer [30, 31]. The increase in *APE* at 100–150 m horizons in T3S5 was consistent with the increased salinity deviations in the two experiments (Fig. 2, *b*).

The higher values of *KE* in the T3S5 experiment in summer at the lower boundary of the thermocline were determined by the structure of the Rim Current (Fig. 3, *d*): for the T2S2 experiment in the western sea part the stream continuity was broken and the jet velocity was about 20% lower (Fig. 3, *c*) compared to the T3S5 data. *In-situ* measurements of current velocities in the northern sea part in 2016 [27], [32] indicated that the jet of the Rim Current with velocities up to 60 cm/s was located above the depth dump, while the generation of eddies and meanders with velocities up to 40 cm/s was observed west of Sevastopol. The analysis of the horizontal velocity fields showed that the T3S5 data (Fig. 3, *d* and Fig. 4, *d*) were more consistent with the real observations. It can be hypothesized that the enhancement of currents and the decrease in *APE* in the upper sea layer in the T3S5 experiment were related to the increase in the energy flux from *APE* to *KE* due to baroclinic instability. However, this hypothesis requires a separate detailed study of the *APE* and *KE* budget components, which is planned in the future.

**Spectral analysis**

Analysis of observational data in the deep Black Sea showed that the balance between the Coriolis force and the pressure gradient was close to quasigeostrophic [33, 34]. According to the theory of quasigeostrophic turbulence, the kinetic energy spectrum changes according to the $k^{-3}$ law [35]. The wavenumber ($k$) spectra were considered to evaluate the energy change at different scales for the two experiments. Model spectral density was calculated from data of the current kinetic energy per unit mass in the upper 100-meter layer of the abyssal sea part (areas with depth more than 200 m). As noted in the analysis of thermohaline characteristics in Section 3.2, the most significant differences in the model results were observed in the second half of the year at 0–100 m horizons (Table 1). Spatial spectra were constructed by averaging the *KE* fields for the year, for the first and for the second half of the year. The most informative averaging interval for the period July 1 – December 31, 2016 was selected to analyze the energy changes at different motion scales. These data are presented in Fig. 9.

The dashed lines in Fig. 9 show the spatial ranges of motions corresponding in the Black Sea to large-scale from 500 to 100 km (b1–b2), mesoscale from 100 to 10 km (b2–b3), and submesoscale less than 10 km (< b3) variabilities. In the T3S5 experiment, the slope of the energy spectrum increased in the b1–b2 range, indicating increase in the relative contribution of large-scale processes to the kinetic energy of the currents compared to T2S2 data. In the b2–b3 range, both experiments showed similar variability, and the slopes of the spectra were consistent with those

predicted theoretically. Decrease in the energy for the T3S5 was observed in the range of submesoscale motions (< b3), hence the contribution of processes acting in the small wavenumber range was reduced.

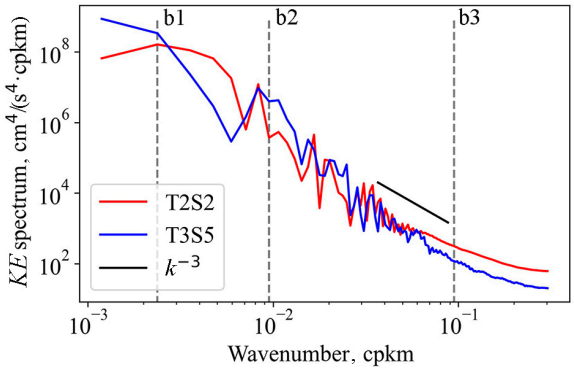


**F i g. 9.** Spectral density of *KE* per unit mass from the experimental results and quasigeostrophic turbulence theory. Dashed lines are ranges of spatial scale of liquid motion: b1 – 500 km; b2 – 100 km; b3 – 10 km

Comparison of the modelling results demonstrated the differences in upwelling/downwelling velocities in the two experiments (Fig. 7). Due to the fact that at quasigeostrophic balance the vertical velocity is a small difference of large numbers, it is a sensitive parameter in the numerical estimation of horizontal current velocities. To evaluate the influence of high-frequency small-scale features on the circulation structure, we analyzed the frequency spectra of the vertical velocity using the fast Fourier transform (the method of [36]) at various points in the basin (Fig. 10) at the 56 m horizon, corresponding to the depth of the maximum vertical velocity according to the results of preliminary experiments (Fig. 8, *b* in [25]. Evaluation of the amplitude heights of the spectra at points 1–5 (Fig. 10) for both experiments showed that the main energy-carrying interval in the deep sea (Fig. 10, points 1, 2) was high-frequency variability with periods of about 2 days, which various authors attribute to mesoscale processes due to the influence of wind [37], pressure fields [38], and eddy dynamics [39].

In the western deep-sea part (Fig. 10, point 1), the spectrogram from the T2S2 data showed two peaks at periods of 2.7 and 2.5 days. According to the T3S5 data, the most energy-carrying period was 2.1 days, which is more in agreement with the estimates of other authors [30, 40]. In the eastern deep-sea part (Fig. 10, point 2), the variability of $w$ was qualitatively similar in the two experiments with some increase in the contribution of vertical oscillations in the high-frequency sector of the spectrum in the T3S5 experiment.

In the coastal zone (Fig. 10, points 3–5), the main energy-carrying interval was low-frequency oscillations with periods of 10–20 days, which corresponded to the characteristics of barotropic topographic Rossby waves over a sloping bottom [41, 42]. Note that the $w$ amplitude in the T3S5 experiment was higher by 25–50% than in T2S2. In the northeastern sea part (Fig. 10, point 4), commensurate amplitudes of low- and high-frequency oscillations were observed in both experiments, indicating significant contribution of both meso- and submesoscale motions to the variability of vertical velocity.

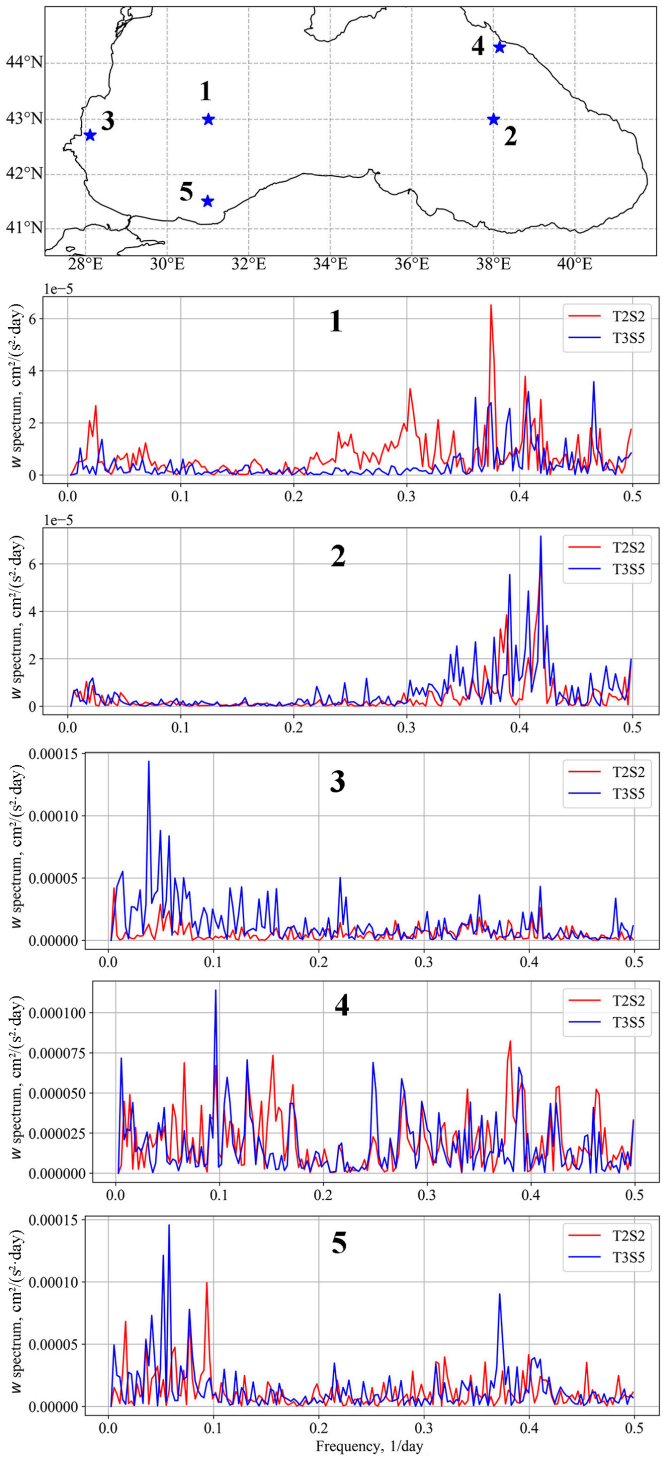


**Fig. 10.** Location of points where *w* frequency spectra are calculated (top). Spectral density of *w* in points 1–5 from the experimental results

In the spectrogram from the T3S5 data, the main contribution to the oscillation energy corresponds to the peak with a period of 11 days, which is usually interpreted as oscillations associated with the Rim Current meandering [43, 44].

In accordance with the continuity condition and under the quasigeostrophic assumption, which is fulfilled with sufficient accuracy in the Black Sea abyssal part [33, 34], the vertical current velocity is proportional to the horizontal pressure gradient. The analysis of the model thermohaline fields in the T3S5 showed an increase in the shore-normal salinity gradients (Fig. 6, *b*, *d*) in the western sea part, which is consistent with the increase in the energy of vertical motions in this domain according to the T3S5 data (Fig. 10, points 3, 5).

In general, the comparison of the frequency spectra for all considered points in the two experiments indicated that the contribution of high-frequency oscillations in the abyssal part and low-frequency oscillations in the coastal zone, as described in the Black Sea research, was more accurately reproduced in the T3S5 experiment than in T2S2. Thus, the application of the new approximation scheme of advective terms in the heat and salt transport equation allowed us to clarify the Black Sea circulation structure thanks to a more accurate redistribution of energy along the spectrum of motions.

## Conclusion

The paper presents a new nonlinear scheme for the approximation of advective terms in the heat and salt transport equations. It provides the conservation of temperature in the first and $K^{\text{th}}$ ($K > 2$) degree, salinity in the first and $L^{\text{th}}$ ($L > 2$) degree. Its distinguishing feature is its compactness since it uses a minimal discrete pattern (three grid points). Another important property is that if the temperature (and/or salinity) in degree $K$ (and/or $L$) is conserved, the corresponding integrals from smaller degrees of temperature (and/or salinity) are bounded. The disadvantages of this approximation include limitations due to its form (a polynomial divided by a polynomial) and the stepwise increase in rounding errors when $K$ (and/or $L$) increases.

In the continuous formulation, if a functional depends on functions that are Lagrangian invariants, then it is itself a Lagrangian invariant. Discrete analogue of such functional solution in a divergence form are given in this paper. In accordance with these results, the finite-difference density equation is derived as an exact consequence of the discrete heat and salt advection equations. It has a divergence form and leads to the same description of the buoyancy work in the discrete kinetic and potential energy equations. These results are valid for transport equations, differential in time and discrete in space, and under the assumption that the continuity equation is fulfilled.

The new scheme is tested on the example of modelling of the Black Sea circulation under realistic atmospheric forcing in 2016. The hydrophysical fields obtained by the new and traditional schemes are compared. The analysis shows that for the Black Sea the new scheme works more correctly in the zone of vertical gradients caused by the evolution of the CIL and permanent halocline. The CIL is sharpened and its depth decreases, and the depth of the upper boundary of the permanent halocline decreases. Comparison of the experimental results with *in-situ* data shows that the modelling error of salinity fields decreases in the upper

100-m layer when the new scheme (22) is used. It is noted that at the end of the year at horizons below 75 m the modelling errors of temperature and salinity fields are significantly smaller compared to the traditional scheme. The decrease in modelling errors is related to the weakening of vertical mixing. It is found that the vertical diffusion coefficient is 2–3 times smaller in the zones with the largest difference of temperature and salinity fields.

The analysis of circulation dynamics and energetics in the two experiments demonstrates that application of the new scheme leads to the following effects. It is found that the Rim Current is more intense in the upper 75-meter layer in spring and summer due to changes in the density field, while the available potential energy in the halocline layer increases due to a more accurate reconstruction of the horizontal salinity gradients between the basin periphery and the abyssal part. The spatial spectra of the kinetic energy in the two experiments show a decrease in the energy of submesoscale perturbation in the second experiment. This result can be interpreted as a reduction in energy redistribution at small scales, which are predisposed to the accumulation of computational noise. Analysis of the frequency spectra of the vertical velocity indicates that both experiments give major energy-carrying motion intervals with periods of 10–18 days and about 2 days, which is consistent with the literature. Herewith, the periods of high-frequency oscillations in the abyssal sea and low-frequency oscillations in the coastal zone are simulated more accurately when the new scheme is used.

Thus, the advantage of the new approximation scheme of advective terms in the heat and salt transport equations is demonstrated by the example of the Black Sea circulation modelling. However, further investigation of the new scheme properties is required for one-dimensional or two-dimensional transport problems having an analytical solution due to the aforementioned limitations.

REFERENCES


1. Roache, P.J., 1976. *Computational Fluid Dynamics*. Albuquerque: Hermosa Publishers, 446 p.
2. Marchuk, G.I., 1982. *Methods of Numerical Mathematics*. Stochastic Modelling and Applied Probability Book Series. New York: Springer-Verlag, 510 p.
3. Blumberg, A.F. and Mellor, G.L., 1983. Diagnostic and Prognostic Numerical Circulation Studies of the South Atlantic Bight. *Journal of Geophysical Research: Oceans*, 88(C8), pp. 4579-4592. https://doi.org/10.1029/JC088iC08p04579
4. Shchepetkin, A.F. and McWilliams, J.C., 2005. The Regional Oceanic Modeling System (ROMS): A Split-Explicit, Free-Surface, Topography-Following-Coordinate Oceanic Model. *Ocean Modelling*, 9(4), pp. 347-404. https://doi.org/10.1016/j.ocemod.2004.08.002
5. Madec, G. and the NEMO System Team, 2023. *NEMO Ocean Engine Reference Manual*. Zenodo, 323 p. https://doi.org/10.5281/zenodo.8167700
6. IOC, SCOR and IAPSO, 2010. *The International Thermodynamic Equation of Seawater – 2010: Calculation and Use of Thermodynamic Properties*. Intergovernmental Oceanographic Commission, Manuals and Guides No. 56. UNESCO, 196 p.
7. Goloviznin, V.M. and Samarskii, A.L., 1998. Finite Difference Approximation of Convective Transport Equation with Space Splitting Time Derivative. *Mathematical Modelling*, 10(1), pp. 86-100 (in Russian).
8. Afanasiev, N.A., Goloviznin, V.M. and Solovjev, A.V., 2021. CABARET Scheme with Improved Dispersion Properties for Systems of Linear Hyperbolic-Type Differential Equations. *Numerical Methods and Programming*, 22(1), pp. 67-76. https://doi.org/10.26089/NumMet.v22r105 (in Russian).

9. Goloviznin, V.M., Maiorov, P.A., Maiorov, P.A. and Solovjev, A.V., 2022. Validation of the Low Dissipation Computational Algorithm CABARET-MFSH for Multilayer Hydrostatic Flows with a Free Surface on the Lock-Release Experiments. *Journal of Computational Physics*, 463, 111239. https://doi.org/10.1016/j.jcp.2022.111239

10. Cacace, S., Cristiani, E. and Ferretti, R., 2017. Blended Numerical Schemes for the Advection Equation and Conservation Laws. *ESAIM: Mathematical Modelling and Numerical Analysis*. 51(3), pp. 997-1019. https://doi.org/10.1051/m2an/2016047

11. Andallah, L.S. and Khatun, M.R., 2020. Numerical Solution of Advection-Diffusion Equation Using Finite Difference Schemes. *Bangladesh Journal of Scientific and Industrial Research*, 55(1), pp. 15-22. https://doi.org/10.3329/bjsir.v55i1.46728

12. Ozbenli, E. and Vedula, P., 2020. Construction of Invariant Compact Finite-Difference Schemes. *Physical Review E*, 101(2), 023303. https://doi.org/10.1103/PhysRevE.101.023303

13. Demyshev, S.G., 1998. Buoyant-Force Approximation in a Numerical Model of Baroclinic Ocean Currents. *Izvestiya, Atmospheric and Oceanic Physics*, 34(3), pp. 362-369.

14. Demyshev, S.G., 2023. Nonlinear Invariants of a Discrete System of the Sea Dynamics Equations in a Quasi-Static Approximation. *Physical Oceanography*, 30(5), pp. 523-548.

15. Bryan, K., 1969. A Numerical Method for the Study of the Circulation of the World Ocean. *Journal of Computational Physics*, 4(3), pp. 347-376. https://doi.org/10.1016/0021-9991(69)90004-7

16. Jouanno, J., Sheinbaum, J., Barnier, B. and Molines, J.-M., 2009. The Mesoscale Variability in the Caribbean Sea. Part II: Energy Sources. *Ocean Modelling*, 26(3–4), pp. 226-239. https://doi.org/10.1016/j.ocemod.2008.10.006

17. Grooms, I., Nadeau, L.-P. and Smith, K.S., 2013. Mesoscale Eddy Energy Locality in an Idealized Ocean Model. *Journal of Physical Oceanography*, 43(9), pp. 1911-1923. https://doi.org/10.1175/JPO-D-13-036.1

18. Fox-Kemper, B. and Marsland, S., 2020. Sources and Sinks of Mesoscale Eddy Energy: Introduction to a CLIVAR/US CLIVAR Special Issue inspired by the March 2019 Workshop in Tallahassee, Florida. *Variations*, 18(1), pp. 1-10. https://doi.org/10.5065/g8w0-fy32

19. Stanev, E.V., 1990. On the Mechanisms of the Black Sea Circulation. *Earth-Science Reviews*, 28(4), pp. 285-319. https://doi.org/10.1016/0012-8252(90)90052-W

20. Cessi, P., Pinardi, N. and Lyubartsev, V., 2014. Energetics of Semienclosed Basins with Two-Layer Flows at the Strait. *Journal of Physical Oceanography*, 44(3), pp. 967-979. https://doi.org/10.1175/JPO-D-13-0129.1

21. Demyshev, S.G. and Dymova, O.A., 2016. Analyzing Intraannual Variations in the Energy Characteristics of Circulation in the Black Sea. *Izvestiya, Atmospheric and Oceanic Physics*, 52(4), pp. 386-393. https://doi.org/10.1134/S0001433816040046

22. Arakawa, A. and Lamb, V.R., 1977. Computational Design of the Basic Dynamical Processes of the UCLA General Circulation Model. *Methods in Computational Physics: Advances in Research and Applications*, 17, pp. 173-265. https://doi.org/10.1016/B978-0-12-460817-7.50009-4

23. Demyshev, S.G. and Dymova, O.A., 2022. Analysis of the Annual Mean Energy Cycle of the Black Sea Circulation for the Climatic, Basin-Scale and Eddy Regimes. *Ocean Dynamics*, 72(3–4), pp. 259-278. https://doi.org/10.1007/s10236-022-01504-0

24. Mellor, G.L. and Yamada, T., 1982. Development of a Turbulence Closure Model for Geophysical Fluid Problems. *Reviews of Geophysics and Space Physic*, 20(4), pp. 851-875. https://doi.org/10.1029/RG020i004p00851

25. Demyshev, S.G. and Dymova, O.A., 2024. Modeling Black Sea Circulation Using Heat and Salt Advection–Diffusion Equations with Discrete Nonlinear Invariants. *Izvestiya, Atmospheric and Oceanic Physics*, 60(2), pp. 195-209. https://doi.org/10.1134/S0001433824700130

26. Mamaev, O.I., 1975. *Temperature-Salinity Analysis of World Ocean Waters*. Elsevier Oceanography Series. Amsterdam: Elsevier Science. Vol. 11, 374 p. https://doi.org/10.1016/s0422-9894(08)x7055-2

27. Artamonov, Yu.V., Skripaleva, E.A., Alekseev, D.V., Fedirko, A.V., Shutov, S.A., Kolmak, R.V., Shapovalov, R.O. and Shcherbachenko, S.V., 2018. Hydrological Research in the Northern Part of the Black Sea in 2016 (87th, 89th and 91st Cruises of R/V Professor Vodyanitsky). *Physical Oceanography*, 25(3), pp. 229-234. https://doi.org/10.22449/1573-160X-2018-3-229-234

28. Poulain, P.-M., Barbanti, R., Motyzhev, S. and Zatsepin, A., 2005. Statistical Description of the Black Sea Near-Surface Circulation Using Drifters in 1999–2003. *Deep-Sea Research Part I: Oceanographic Research Papers*, 52(12), pp. 2250-2274. https://doi.org/10.1016/j.dsr.2005.08.007

29. Bulgakov, S.N. and Korotaev, G.K., 1984. Possible Mechanism of Stationary Circulation of Black Sea Waters. In: MHI, 1984. *Integrated Research of the Black Sea*. Sevastopol: MHI, pp. 32-40 (in Russian).

30. Ivanov, V.A. and Belokopytov, V.N., 2013. *Oceanography of the Black Sea*. Sevastopol: ECOSI-Gidrofizika, 210 p.

31. Demyshev, S., Dymova, O. and Miklashevskaya, N., 2022. Seasonal Variability of the Dynamics and Energy Transport in the Black Sea by Simulation Data. *Water*, 14(3), 338. https://doi.org/10.3390/w14030338

32. Morozov, A.N. and Mankovskaya, E.V., 2019. Seasonal Variability of Currents Structure in the Black Sea Northern Part from Field Measurements in 2016. *Fundamental and Applied Hydrophysics*, 12(1), pp. 15-20. https://doi.org/10.7868/S2073667319010027 (in Russian).

33. Kubryakov, A.A. and Stanichny, S.V., 2013. Estimating the Quality of the Retrieval of the Surface Geostrophic Circulation of the Black Sea by Satellite Altimetry Data Based on Validation with Drifting Buoy Measurements. *Izvestiya, Atmospheric and Oceanic Physics*, 49(9), pp. 930-938. https://doi.org/10.1134/S0001433813090089

34. Menna, M. and Poulain, P.-M., 2014. Geostrophic Currents and Kinetic Energies in the Black Sea Estimated from Merged Drifter and Satellite Altimetry Data. *Ocean Science*, 10(2), pp. 155-165. https://doi.org/10.5194/os-10-155-2014

35. Stammer, D., 1997. Global Characteristics of Ocean Variability Estimated from Regional TOPEX/POSEIDON Altimeter Measurements. *Journal of Physical Oceanography*, 27(8), pp. 1743-1769. https://doi.org/10.1175/1520-0485(1997)027<1743:GCOOVE>2.0.CO;2

36. Welch, P., 1967. The Use of the Fast Fourier Transform for the Estimation of Power Spectra: A Method Based on Time Averaging over Short, Modified Periodograms. IEEE *Transactions on Audio and Electroacoustics*, 15(2), pp. 70-73. https://doi.org/10.1109/TAU.1967.1161901

37. Goryachkin, Yu.N. and Ivanov, V.A., 2006. [*Level of the Black Sea: Past, Present and Future*]. Sevastopol: ECOSI Gidrofizika, 210 p. (in Russian).

38. Medvedev, I.P., 2022. Numerical Modeling of Meteorological Sea Level Oscillations in the Black Sea. *Oceanology*, 62(4), pp. 471-481. https://doi.org/10.1134/S0001437022040087

39. Zhurbas, V.M., Zatsepin, A.G., Grigor'eva, Yu.V., Poyarkov, S.G., Eremeev, V.N., Kremenetsky, V.V., Motyzhev, S.V., Stanichny, S.V., Soloviev, D.M. [et al.], 2004. Water Circulation and Characteristics of Currents of Different Scales in the Upper Layer of the Black Sea from Drifter Data. *Oceanology*, 44(1), pp. 30-43.

40. Stanev, E.V. and Beckers, J.M., 1999. Barotropic and Baroclinic Oscillations in Strongly Stratified Ocean Basins. *Journal of Marine Systems*, 19(1–3), pp. 65-112. https://doi.org/10.1016/S0924-7963(98)00024-4

41. Blatov, A.S., Bulgakov, N.P., Ivanov, V.A., Kosarev, A.N. and Tuzhilkin, V.S., 1984. *Variability of the Black Sea Hydrophysical Fields*. Leningrad: Gydrometeoizdat, 240 p. (in Russian).

42. Aydın, M. and Beşiktepe, Ş.T., 2022. Mechanism of Generation and Propagation Characteristics of Coastal Trapped Waves in the Black Sea. *Ocean Science*, 18(4), pp. 1081-1091. https://doi.org/10.5194/os-18-1081-2022

43. Zatsepin, A.G., Elkin, D.N., Korzh, A.O., Kuklev, S.B., Podymov, O.I., Ostrovskii, A.G. and Soloviev, D.M., 2016. On Influence of Current Variability in the Deep Black Sea upon Water Dynamics of Narrow North Caucasian Continental Shelf. *Physical Oceanography*, (3), pp. 14-22. https://doi.org/10.22449/1573-160X-2016-3-14-22

44. Kuznetsov, A.S., 2020. Structure of the Coastal Current Direction Bimodality at the Southern Coast of Crimea in 2002–2008. *Ecological Safety of Coastal and Shelf Zones of Sea*, (4), pp. 78-88. https://doi.org/10.22449/2413-5577-2020-4-78-88

Submitted 09.07.2025; approved after review 16.08.2025;
accepted for publication 10.11.2025.

*About the authors*:

**Sergey G. Demyshev**, Head of Wave Theory Department, Senior Researcher, Marine Hydrophysical Institute of RAS (2 Kapitanskaya Str., Sevastopol, 299011, Russian Federation), DSc. (Phys.-Math.), **Scopus Author ID: 6603919865**, **SPIN-code: 1848-2350**, **ResearcherID: C-1729-2016**, **ORCID ID: 0000-0002-5405-2282**, demyshev@gmail.com

**Olga A. Dymova**, Leading Researcher, Marine Hydrophysical Institute of RAS (2 Kapitanskaya Str., Sevastopol, 299011, Russian Federation), CSc. (Phys.-Math.), **Scopus Author ID: 6508381809, ResearcherID: P-9669-2015**, **ORCID ID: 0000-0003-4036-2447**, olgdymova@mhi-ras.ru

*Contribution of the co-authors*:

**Sergey G. Demyshev** – review of literature on the research problem; designation of methodological basis of the study; formulation of aims and objectives; development of a mathematical model; discussion of the study results; editing and supplementing the text; critical analysis and revision of the text

**Olga A. Dymova** – review of literature on the research problem; carrying out calculations for the Black Sea; processing and description of results for the Black Sea; analysis of results and their interpretation; preparation of the text; data visualization/presentation in the text

*The authors have read and approved the final manuscript.*
*The authors declare that they have no conflict of interest.*